Supplementary Information on the manuscript:

Monitoring the multiphasic evolution of bismuth telluride nanoplatelets

Ahmed Subrati, [a,b] Yeonho Kim, [c,d] Yasser Al Wahedi, [a,e] Vasileios Tzitzios, [a,f] Saeed Alhassan, [a*] Hae Jin Kim, [c*] Sanggil Lee, [c] Elias Sakellis, [f] Nikos Boukos, [f] Samuel Stephen, [a] Sang Moon Lee, [c] Jin Bae Lee, [c] Michael Fardis, [f] and Georgios Papavassiliou [f*]

[a]Department of Chemical Engineering, Khalifa University of Science and Technology, Abu Dhabi, 127788, UAE

[b]NanoBioMedical Centre, Adam Mickiewicz University, Wszechnicy Piastowskiej 3, 61614 Poznan, Poland

[c]Electron Microscopy Research Center, Korea Basic Science Institute, Daejeon 34133, Republic of Korea

[d]Research Institute of Basic Sciences, Incheon National University, Incheon 22012, Republic of Korea

[e]Center for Catalysis and Separation, Khalifa University of Science and Technology, P.O.Box 127788, Abu Dhabi, UAE

[f]Institute of Nanoscience and Nanotechnology, National Center for Scientific Research 'Demokritos', Agia Paraskevi, Attiki, Greece

The supplementary information comprises details of Rietveld refinements, FTIR, BET, UV-vis, TGA, EDS/TEM, and HR-TEM results of synthesized samples of bismuth telluride.

Stoichiometric Bi$_2$Te$_3$ nanoplatelets

1) Rietveld refinement

All stoichiometry-default patterns were realistically fit to the single tellurobismuthite (Bi$_2$Te$_3$) phase except S-5, where a theoretical pattern was used consisting of three phases: tsumoite (BiTe), pilsenite (Bi$_4$Te$_3$) and tellurobismuthite (Bi$_2$Te$_3$). Refined parameters include: scale factor, background points (BGP) using linear interpolation, lattice parameters, atomic positions, size effects, asymmetry parameters and preferred orientation. Tables S1 and S2 include the refinement results of S-1 and S-5, respectively.

Table S1 Rietveld refinement summary of S-1.

**Tellurobismuthite (Bi$_2$Te$_3$)** contribution: 100%						
Atom	**Site**	**x (Å)**	**y(Å)**	**z (Å)**	**B (J)**	**Occupancy**
Te2	3a	0.00000	0.00000	0.00000	1.38000	0.08333
Bi	6c	0.00000	0.00000	0.40023	1.84000	0.16667
Te1	6c	0.00000	0.00000	0.79043	1.51000	0.16667
Lattice parameters: a = 4.38315 Å, b = 4.38315 Å, c = 30.54567 Å, $\alpha = \beta = 90°$, $\gamma = 120°$						
Weighted R factors: R$_{wp}$ = 5.05, R$_p$ = 4.92, $\chi^2 = 1.54$						

2) FTIR, BET, UV-vis and TGA results for pristine bismuth telluride

Figure S1 shows the FTIR spectra of pure PVP and pristine Bi_2Te_3. Spectral comparative analysis confirms modest presence of the organic capping agent (PVP) on Bi_2Te_3, which is sufficient to prevent agglomeration of nanoplatelets as mass agglomeration is anticipated if the nanoplatelets are capping agent free[1]. The broad bands, in pure PVP (Figure S1A) and PVP-functionalized Bi_2Te_3 nanoplatelets (Figure S1B), around 3400 cm^{-1} are attributed to O-H stretching from hydrogen bonded water while the bands around 2900 cm^{-1} are assigned to the symmetric and asymmetric C-H stretches. Shoulder bands have been red-shifted and blue-shifted due to the action of intrinsic Bi_2Te_3 surface plasmons[2]. The bands situated at 668 cm^{-1} and 2357 cm^{-1} (Figure S1B) are attributed to bending and stretching of C=O (of adsorbed atmospheric CO_2), respectively. Both samples exhibit pronounced bands at 1641 cm^{-1} (Figure S1A) and 1636 cm^{-1} (Figure S1B), that correspond to the C=O (carbonyl) stretching vibrations of pure and adsorbed PVP, respectively. This band shifted from 1641 to 1636 cm^{-1} indicating that PVP interacts with the material surface through carbonyl group. C-N bending vibrations of pure PVP appear at 1017 cm^{-1} and 1287 cm^{-1}. Similar vibrations appear for adsorbed PVP at 1262 cm^{-1}. The band located at 1420 cm^{-1} is attributed to -CH_2- bending and rocking vibrations[3-5]. A distinct band at 1034 cm^{-1} is attributed to Bi[3].
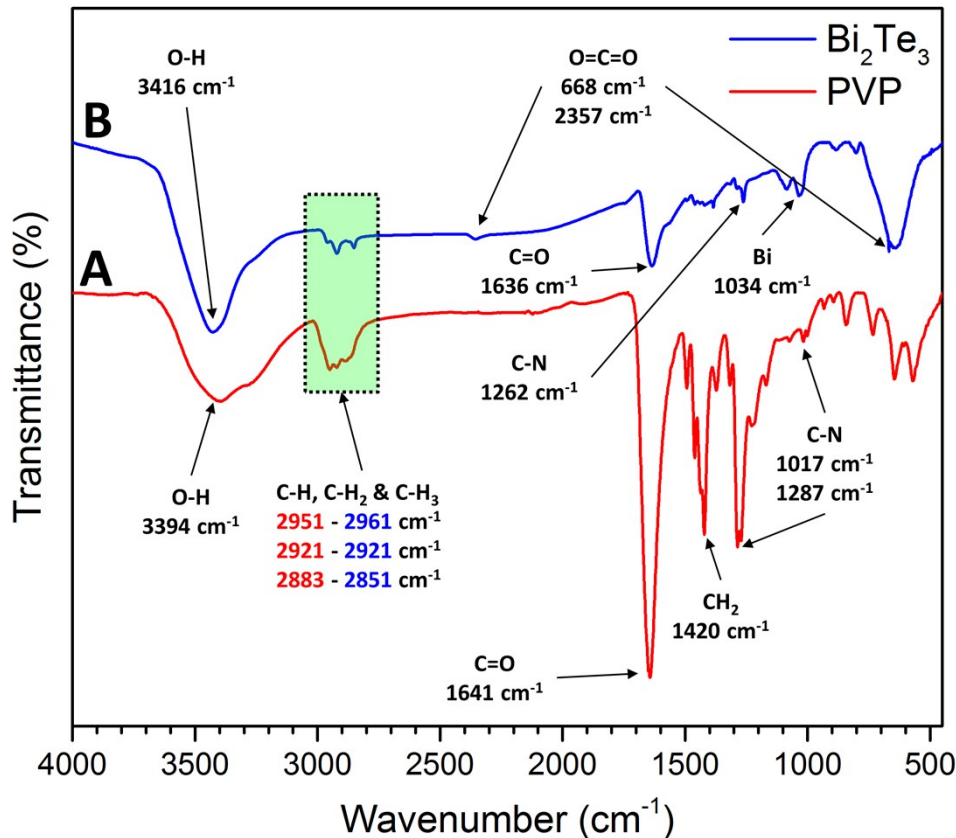
Figure S1 FTIR spectra of pure (A) PVP and (B) Bi_2Te_3.

The produced nanoplatelets are non-porous as confirmed by BET measurement of S-7. The BET surface area of S-7 is ~6.7 m^2/g. Although a typical stable non-porous material exhibits identical pathways of reversible adsorption and desorption, a minor hysteresis loop can be observed around relative pressure of 0.8 (Figure S2A). The loop can be attributed to either imperfect outgassing[6] or presence of surface impurities[7]. Elimination of such artifact could be done through repetition of adsorption and desorption cycles[6].

Bi_2Te_3 exhibits a strong and broad absorption spectrum that extends in the visible range of 400–700 nm (see Figure S2B) as reported in other studies[2]. The absorption pattern of Bi_2Te_3 can be attributed to the visible plasmons that are an innate feature of a typical TI as they evolve as a result of the TSSs that are an ultimate consequence of strong SOC[2], where the electron spins are strongly locked/coupled to their own momentum. As a result,

the electron spin is locked to its momentum and the backscattering induced by nonmagnetic impurities is prohibited.

The TGA thermogram of Bi_2Te_3 sample S-7 exhibits an initial drop in mass (~1.66%) below 250 °C (Figure S2C, inset), that is attributed to moisture (water) loss from the sample. In the interval of 250-350 °C, there exists a relatively sharper drop in mass (~4.74%) and is attributed to the thermal decomposition of adsorbed PVP[8]. In the interval of 575-825 °C, the sharpest drop in mass occurs (~10.75%) and is attributed to the thermal decomposition of Bi_2Te_3 nanoplatelets as their melting point is 585 °C[9]. Overall, as Figure S2C illustrates, the total mass loss is only ~18.39% upon heating up to 825 °C. Results obtained herein are comparable to those reported in the literature[10].
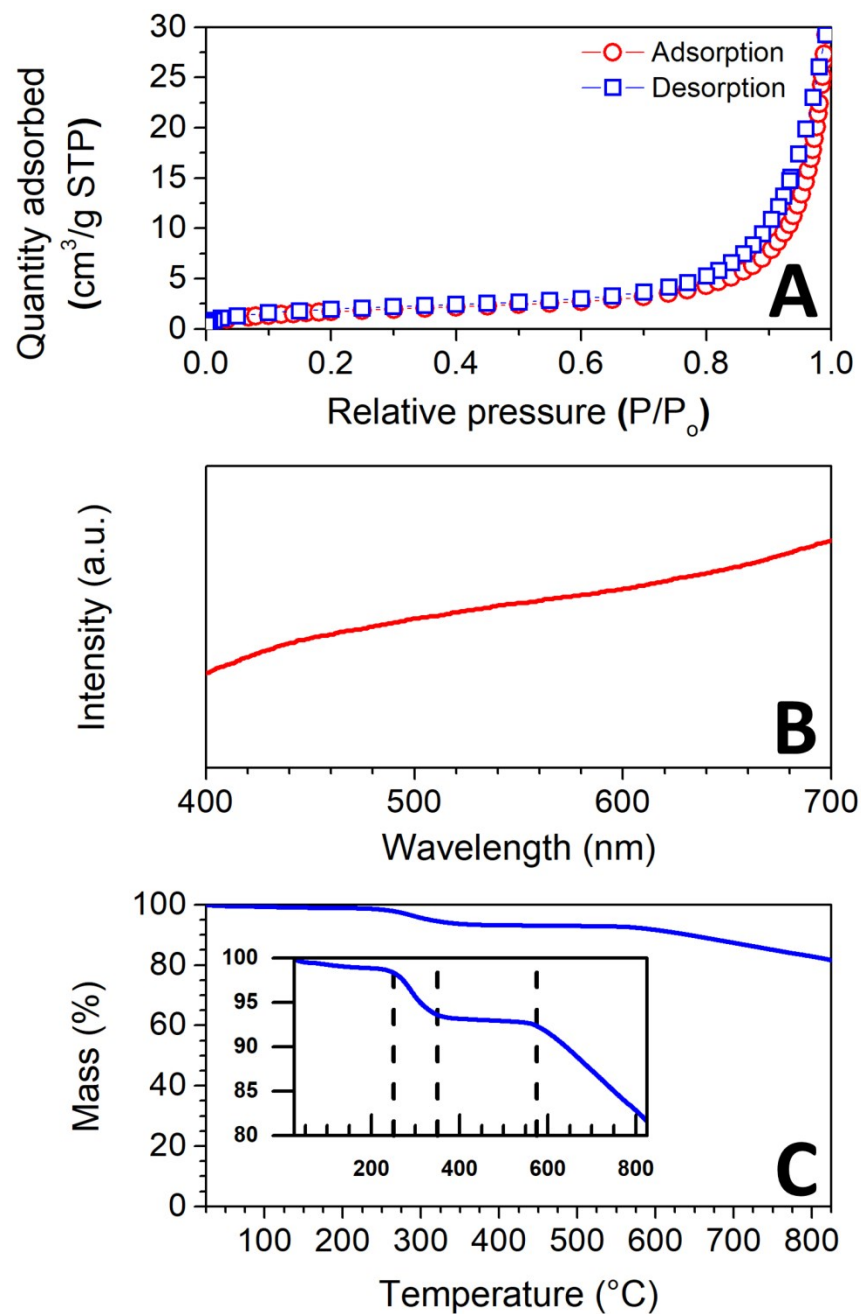
Figure S2 Pristine Bi_2Te_3 nanoplatelets (S-7): (A) BET, (B) UV-vis and (C) TGA (Inset shows the pronounced mass percentage loss within the 80-100% range) measurements.

Bi-rich Bi$_2$Te$_3$ nanoplatelets

1) Rietveld refinement

Table S2 Rietveld refinement summary of S-5.

Tsumoite (BiTe) contribution: 39.20(0.73)%						
Atom	**Site**	**x (Å)**	**y(Å)**	**z (Å)**	**B (J)**	**Occupancy**
Bi1	2c	0.00000	0.00000	0.11985	0.00000	0.16667
Bi2	2d	0.33333	0.66667	0.30089	0.00000	0.16667
Bi3	2d	0.66667	0.33333	0.45984	0.00000	0.16667
Te1	2d	0.33333	0.66667	0.04987	0.00000	0.16667
Te2	2d	0.66667	0.33333	0.21182	0.00000	0.16667
Te3	2c	0.00000	0.00000	0.37724	0.00000	0.16667

Lattice parameters: a = 4.43401 Å, b = 4.43401 Å, c = 24.03554 Å, $\alpha = \beta = 90°$, $\gamma = 120°$

Weighted R factors: R$_{wp}$ = 6.33, R$_p$ = 6.83, χ^2 = 2.13

Pilsenite (Bi$_4$Te$_3$) contribution: 17.45(0.57)%						
Atom	**Site**	**x (Å)**	**y(Å)**	**z (Å)**	**B (J)**	**Occupancy**
Bi1	6c	0.66667	0.33333	0.04810	0.00000	0.16667
Bi2	6c	0.00000	0.00000	0.13592	0.00000	0.16667
Te1	3a	0.00000	0.00000	0.00000	0.00000	0.08333
Te2	6c	0.33333	0.66667	0.08806	0.00000	0.16667

Lattice parameters: a = 4.50396 Å, b = 4.50396 Å, c = 41.25757 Å, $\alpha = \beta = 90°$, $\gamma = 120°$

Weighted R factors: R$_{wp}$ = 10.3, R$_p$ = 8.70, χ^2 = 2.13

Tellurobismuthite (Bi$_2$Te$_3$) contribution: 43.36(1.01)%						
Atom	**Site**	**x (Å)**	**y(Å)**	**z (Å)**	**B (J)**	**Occupancy**
Te2	3a	0.00000	0.00000	0.00000	1.38000	0.08333
Bi	6c	0.00000	0.00000	0.39815	1.84000	0.16667
Te1	6c	0.00000	0.00000	0.78968	1.51000	0.16667

Lattice parameters: a = 4.39411 Å, b = 4.39411 Å, c = 30.33120 Å, $\alpha = \beta = 90°$, $\gamma = 120°$

Weighted R factors: R$_{wp}$ = 6.70, R$_p$ = 5.65, χ^2 = 2.13

2) EDS/TEM

The different phases are distinguished by two numbers, e.g. (23), (11), (32) and (43) represent the Bi_2Te_3, $BiTe$, Bi_3Te_2 and Bi_4Te_3 phases, respectively.

Bismuth and tellurium atomic distributions were sometimes homogeneous and therefore their mappings were not included in some EDS results. All the EDS/TEM results are compiled and approximate phases were assigned accordingly in Table S3. Point analyses of the S-4 agglomerate confirm various compositions although the overall agglomerate's composition is consistent with the stoichiometric Bi_2Te_3 as shown in Figure S3(a-b). A single S-4 nanoplatelet appears in Figure S3c consisting of the (23) phase solely. Two nanoplatelets on top of each other exhibit the (23) phase as well as in Figure S3d. S-4 is mostly consistent of the (23) phase (Figure S3) and thus the effect of lower telluride content was not significantly obvious. However, there was a trace of the (11) phase which could be attributed to the lower telluride content.

S-5 is the bismuth rich sample and this is evident as the (11) and (32) phases were confirmed along with the (23) phase (Figure S4). Point analysis of the nanoplatelet in Figure S4(a) confirmed uniform (23) phase. Figure S4b, however, shows a nanoplatelet with (11) dominant phase that is attributed to the underlying parallelogram nanoplatelet that certainly has very high bismuth content and this is further confirmed by the elemental mapping of bismuth for that nanoplatelet (Figure S4b lower inset). Similar phase is exhibited by the nanoplatelet shown in Figure S4c where probably high bismuth content was detected from the underlying parallelogram nanoplatelet as the lower inset elucidates. The agglomerate analyzed in Figure S4d had the highest bismuth content, representing the (32) phase. Figure S4e presents a default stoichiometric

nanoplatelet with underlying fringes of a dissolved nanoplatelet. The latter fringes contributed to the higher bismuth content. Point analyses of the two nanoplatelets shown in Figure S4(f-g) confirm the following: (1) Smaller nanoplatelets ($\leq$ 400 nm) often exhibit a bismuth-rich phase. (2) Non-uniformly grown hexagonal nanoplatelet possesses dominant bismuth-rich phase, like the (32) phase (spectrum 13). The latter phase presence can be attributed to the underlying truncated hexagonal (rhombus-like) nanoplatelet which may consist of high bismuth content (e.g. the (43) phase for instance).

S-6 exhibited the default (23) (Figure S5b) phase in addition to a tellurium-rich phase; the (12) phase. Figure S5a shows the (12) phase nanoplatelet and the atomic mapping of Te clearly shows a higher density compared to that of Bi. Point analyses of the agglomerate confirm the following: (1) Relatively big (> 700 nm) ultrathin hexagonal nanoplatelet with the (12) phase (spectrum 17). (2) Regular-sized nanoplatelet with the (23) phase (spectrum 18). (3) Non-uniformly grown hexagonal nanoplatelet possesses dominant tellurium-rich phase (12) (spectrum 19). (4) Overall (12) phase of the five nanoplatelets stacking (spectrum 20).
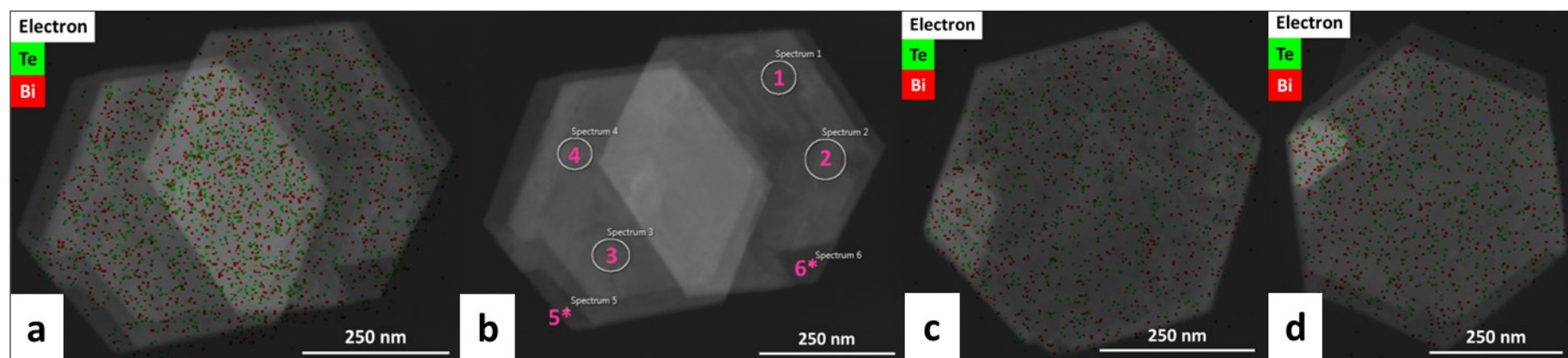
Figure S3 EDS analyses of S-4. (a): site 1, (b): point analysis 1 (spectra 1-6), (c): site 2 and (d): site 3.
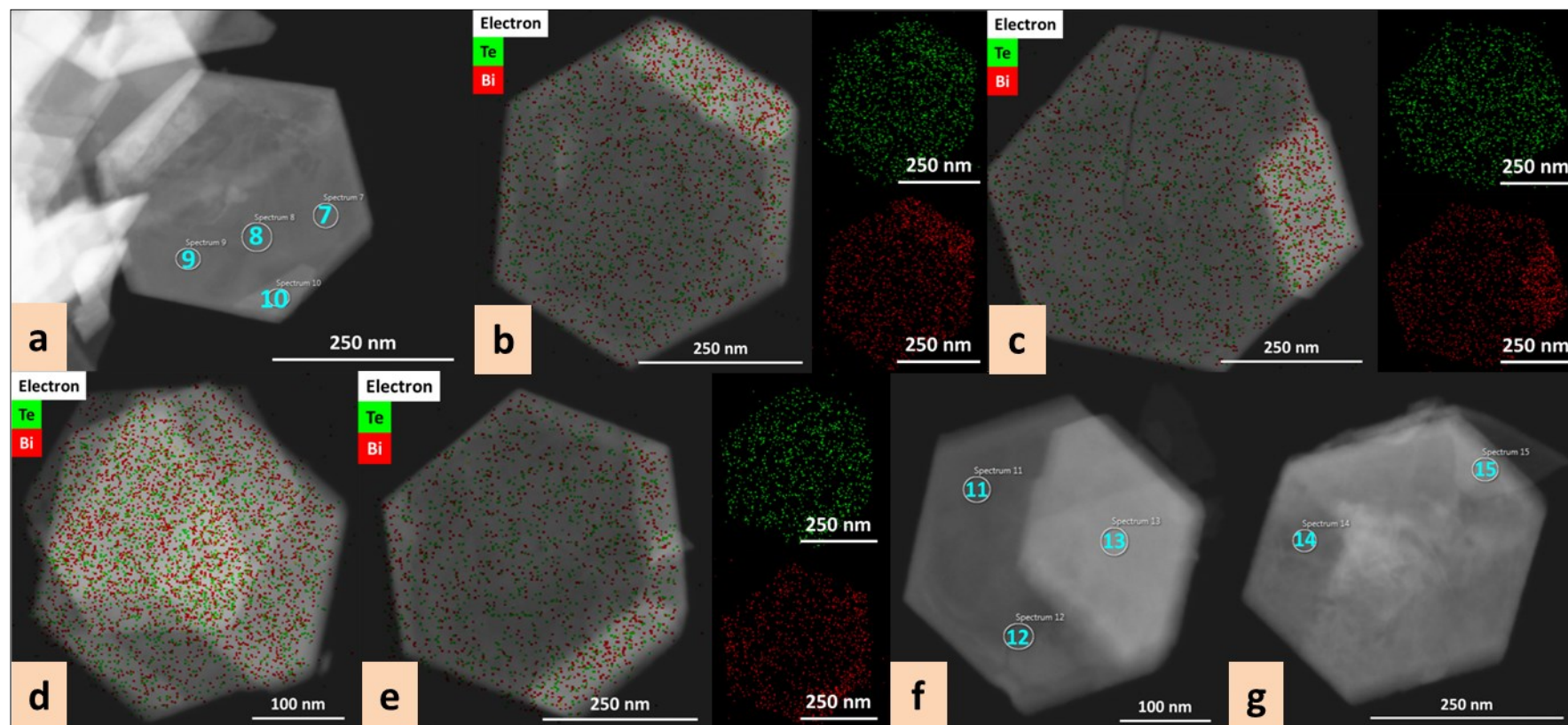
Figure S4 EDS analyses of S-5. (a): point analysis 2 (spectra 7-10), (b): site 4, (c): site 5, (d): site 6, (e): site 7, (f): point analysis 3 (spectra 11-13) and (g): point analysis 4 (spectra 14-15).
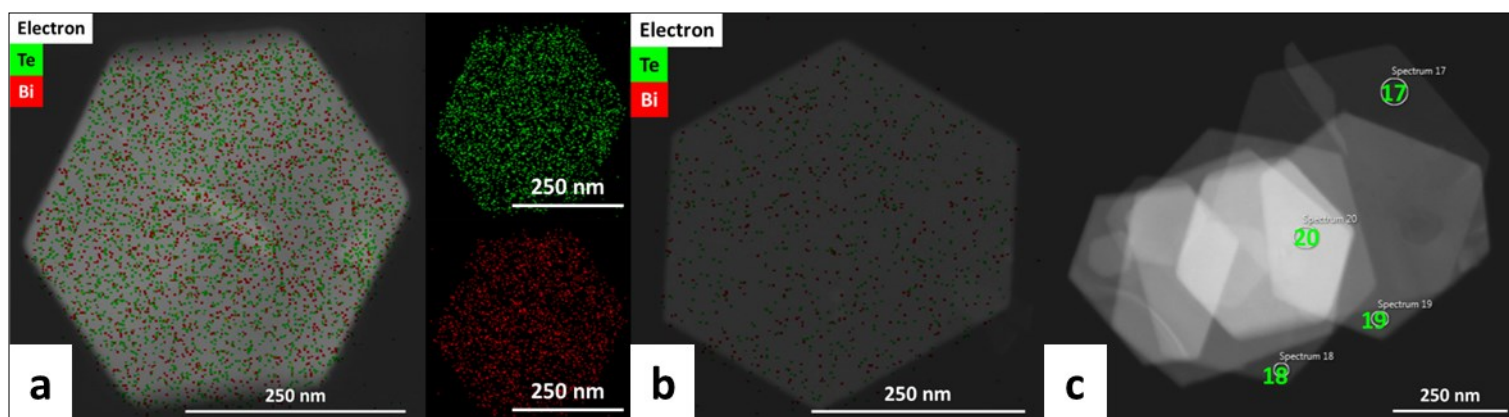
Figure S5 EDS analyses of S-6. (a): site 8, (b): site 9 and (c): point analysis 5 (spectra 17-20).

Table S3 Summary of all EDS/TEM results (S: spectrum).

| Sample	Scan name & number		Atomic composition (%)		Approximate phase
			Bi	Te	
S-4	Site 1		40.70	59.30	(23)
	Point analysis 1	S1	38.51	61.49	(23)
		S2	47.64	52.36	(11)
		S3	40.06	59.94	(23)
		S4	43.30	56.70	(23)
		S5	44.05	55.95	(45)
		S6	41.77	58.23	(23)
	Site 2		39.60	60.40	(23)
	Site 3		41.70	58.30	(23)
S-5	Point analysis 2	S7	38.78	61.22	(23)
		S8	36.72	63.28	(23)
		S9	43.05	56.95	(23)
		S10	41.72	58.28	(23)
	Site 4		48.00	52.00	(11)
	Site 5		48.30	51.70	(11)
	Site 6		56.30	43.70	(32)
	Site 7		47.00	53.00	(11)
	Point analysis 3	S11	49.02	50.98	(11)
		S12	49.01	50.99	(11)
		S13	61.97	38.03	(32)
	Point analysis 4	S14	48.33	51.67	(11)
		S15	53.65	46.35	(11)
S-6	Site 8		33.90	66.10	(12)
	Site 9		38.00	62.00	(23)
	Point analysis 5	S17	33.38	66.62	(12)
		S18	38.31	61.69	(23)
		S19	31.27	68.73	(12)
		S20	35.57	64.43	(12)
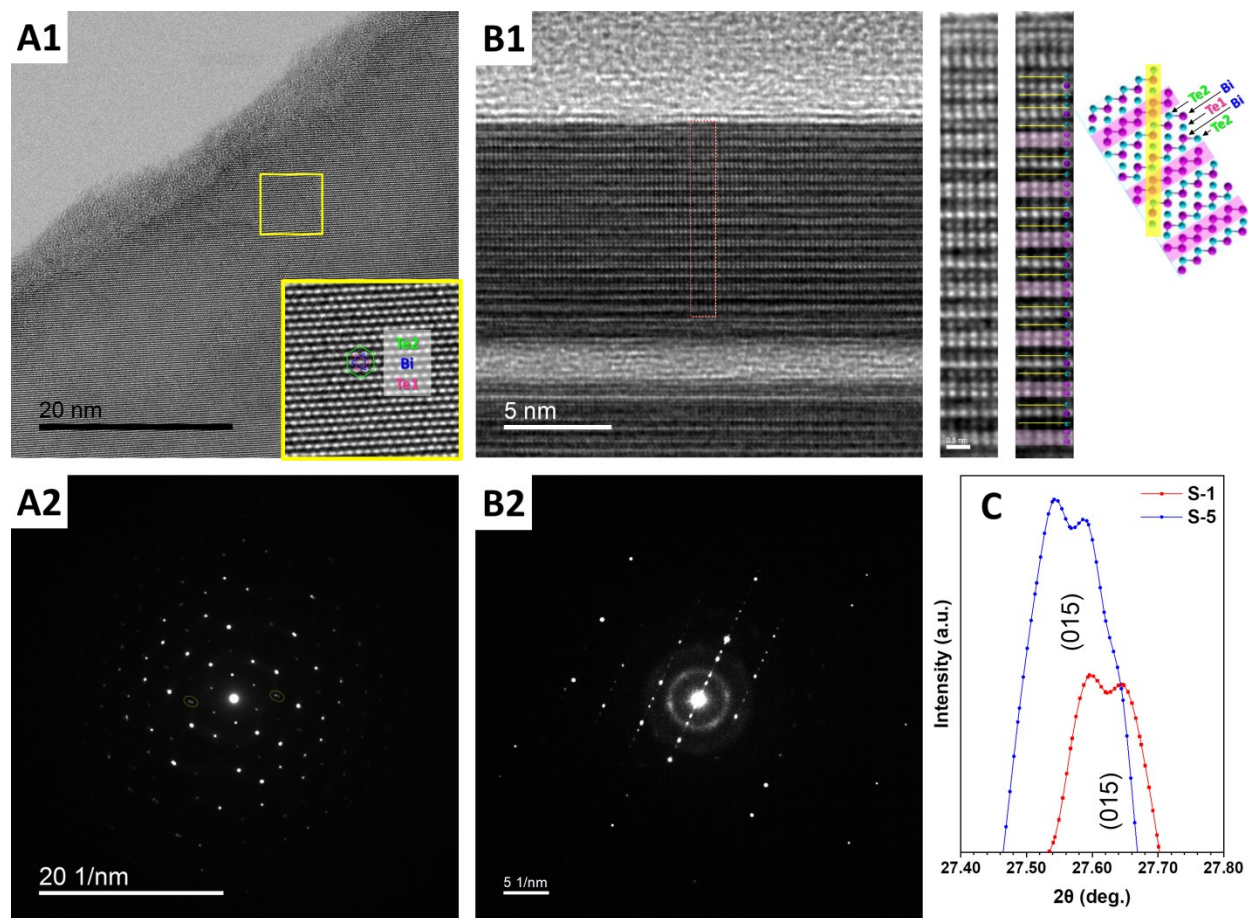
Figure S6 (A1) HR-TEM image of S-1 nanoplatelet depicting the (0001) facet. The inset shows the reconstruction of facet using three layers in the order Te2-Bi-Te1. (A2) Electron diffraction pattern reveals hexagonal peaks and superior order reflections while a twinning feature was observed (split spots) and outlined in dashed yellow ovals. (B1) HR-TEM tilted cross-section view of S-5 nanoplatelet unveiling a ~9.9 nm thick section. Insets show arrangement of atoms: Bi (magenta) and Te (cyan) to construct a Bi_4Te_3 cell. (B2) Electron diffraction pattern of the S-5 nanoplatelet. (C) Close-up view of the (015) diffraction peak of samples S-1 and S-5, the most intense peak in both samples, depicting splitting of their maxima. The splitting infers about existence of two or more orientations (twins) in the lattice.

References

1. M. Loor, G. Bendt, U. Hagemann, C. Wolper, W. Assenmacher and S. Schulz, *Dalton transactions*, 2016, **45**, 15326-15335.

2. M. Zhao, M. Bosman, M. Danesh, M. Zeng, P. Song, Y. Darma, A. Rusydi, H. Lin, C. W. Qiu and K. P. Loh, *Nano letters*, 2015, **15**, 8331-8335.

3. K. Sharma, A. Kumar, N. Goyal and M. Lal, 2013, DOI: 10.1063/1.4810371, 603-604.

4. K. M. Koczkur, S. Mourdikoudis, L. Polavarapu and S. E. Skrabalak, *Dalton transactions*, 2015, **44**, 17883-17905.

5. P. Srivastava and K. Singh, *Journal of Experimental Nanoscience*, 2013, **9**, 1064-1074.

6. K. S. W. Sing and R. T. Williams, *Adsorption Science & Technology*, 2016, **22**, 773-782.

7. E. M. Voigt and R. H. Tomlinson, *Canadian Journal of Chemistry*, 1955, **33**, 215-231.

8. B. Caratão, E. Carneiro, P. Sá, B. Almeida and S. Carvalho, *Journal of Nanotechnology*, 2014, **2014**, 1-5.

9. E. PoŽEga, S. Ivanov, Z. Stević, L. Karanović, R. Tomanec, L. GomidŽElović and A. Kostov, *Transactions of Nonferrous Metals Society of China*, 2015, **25**, 3279-3285.

10. S. M. Kang, S.-S. Ha, W.-G. Jung, M. Park, H.-S. Song, B.-J. Kim and J.-I. Hong, *AIP Advances*, 2016, **6**, 025110.